

2021-12-13

A global atlas of artificial light at night under the sea

Smyth, T

<http://hdl.handle.net/10026.1/18397>

10.1525/elementa.2021.00049

Elementa: Science of the Anthropocene

BioOne

All content in PEARL is protected by copyright law. Author manuscripts are made available in accordance with publisher policies. Please cite only the published version using the details provided on the item record or document. In the absence of an open licence (e.g. Creative Commons), permissions for further reuse of content should be sought from the publisher or author.

A global atlas of artificial light at night under the sea

T. J. Smyth^{1*}, A. E. Wright¹, D. McKee^{2,3}, S. Tidau^{4†,5}, R. Tamir^{6,7}, Z. Dubinsky⁶, D. Iluz^{6,8}, T. W. Davies^{4†,5}

1. Plymouth Marine Laboratory, Prospect Place, Plymouth, Devon, UK, PL1 3DH
2. Physics Department, University of Strathclyde, 107 Rottenrow, Glasgow, Scotland, G4 0NG
3. Department Arctic and Marine Biology, Faculty for Bioscience, Fisheries and Economy, UiT The Arctic University of Norway, Tromsø, Norway
4. School of Biological and Marine Sciences, University of Plymouth, Drake Circus, Plymouth, UK, PL4 8AA
5. School of Ocean Sciences, University of Bangor, Menai Bridge, Anglesey, UK, LL59 5AB
6. The Mina & Everard Goodman Faculty of Life Sciences, Bar-Ilan University, Ramat-Gan 5290002, Israel
7. The Interuniversity Institute for Marine Sciences of Eilat, Eilat, Israel
8. Department of Environmental Sciences and Agriculture, Beit Berl Academic College, Israel

* *Corresponding author: tjasm@pml.ac.uk*

† *Present address*

Abstract

The impacts of artificial light at night (ALAN) on marine ecosystems have emerged as a focus for ecological light pollution research in recent years, yet the global prevalence of ALAN in underwater marine ecosystems is unknown. We have derived a global atlas of ALAN throughout the marine water column that will accelerate our understanding of its sources and environmental impacts. At a depth of 1 m, 1.9 million km² of the world's coastal seas are exposed to biologically important ALAN, which equates to around 3.1% of the global Exclusive Economic Zones. This area decreases to 1.6 million km² (2.7%) at a depth of 10 m, and to 840,000 km² (1.4%) at 20 m. The most heavily exposed regions are those that experience intensive offshore development in addition to coastal urbanization. The atlas highlights that ALAN as a global change issue is not exclusive to land but is also widespread in the world's underwater habitats at irradiances that elicit biological responses in marine organisms.

Introduction

The 21st century will see dramatic increases in coastal urbanization (Neumann et al., 2015) and offshore infrastructure. Lighting from coastal urban centers, oil platforms and other offshore structures scatters in the atmosphere to form artificial skyglow that increases the extent of light pollution from source to hundreds of kilometers into the surrounding marine habitats. The impacts of this light on marine ecosystems has emerged as a focus for ecological light pollution research (Davies et al., 2014; Ludvigsen et al., 2018; Fobert et al., 2019; Torres et al., 2020).

One of the clearest demonstrations that we have entered another epoch, the urbanocene (West, 2018), is the prevalence of artificial light at night (ALAN) visible from space (Falchi et al., 2016a). Satellite-derived

images of the world's night-time lights have been successfully coupled with atmospheric light dispersion models to produce new insights into the prevalence and growth of ALAN skyglow on land (Falchi et al., 2016a; Kyba et al., 2017). Much of this light will enter the world's seas and oceans, which until now has been difficult to quantify. The spectral signature of land-based light sources is detectable on the biodiverse coral reef ecosystems of the Red Sea (Tamir et al., 2017), and radiative transfer modelling of in-water ALAN skyglow transmission suggests that up to three quarters of the seafloor adjacent to cities can be exposed to artificial light irradiances sufficient to elicit biological responses (Davies et al., 2020). Satellite products of the world's night-time lights have proved valuable for quantifying trends in ALAN (Bennie et al., 2014; Kyba et al., 2017), and exposure in terrestrial ecosystems (Mazor et al., 2013; Duffy et al., 2015; McLaren et al., 2018) and protected areas (Gaston et al., 2015). Skyglow-like light levels can affect melatonin in freshwater fish (Kupprat et al., 2020) and more generally impact freshwater ecosystems (Jechow and Hölker, 2019). To date, there is no atlas of the extent of ALAN under the sea, limiting advances in understanding and quantifying the impacts of marine ALAN from the organism to ecosystem level.

We have derived a high-resolution global atlas of ALAN under the sea. The atlas is produced at a spatial scale of approximately 1 km x 1 km by combining the recently available world atlas of artificial night sky brightness (Falchi et al., 2016a; 2016b), satellite-derived in-water spectral optical properties (Lee et al., 2002), sea surface-measured artificial light irradiances (Davies et al., 2020) and hydrological radiative transfer modelling (Mobley, 1995) (Figure 1). The atlas is calibrated using derived relationships between artificial sky brightness (Falchi et al., 2016a) and broadband sea surface irradiances (blue, nominally 400–500 nm; green, nominally 500–600 nm; and red, nominally 600–700 nm) collected from waters adjacent to the city of Plymouth, UK (Davies et al., 2020) (Table 1). To model attenuation of light in the three wavebands, inherent optical properties (IOPs: absorption due to phytoplankton, colored dissolved organic matter (CDOM) and particulates, and backscatter due to particulates) were derived using global monthly climatologies (1998–2017) calculated from the primary IOP dataset of the European Space Agency Climate Change Initiative (Sathyendranath et al., 2019a; 2019b). The resulting broadband irradiances were then integrated to produce absolute irradiances of ALAN underwater with depth. This approach allowed insight for the first time into the spatial extent of in-water marine light pollution and its temporal variability on a global scale.

To understand the biological importance of the modelled underwater ALAN field, we calculated the critical depth (Z_c) to which biologically important ALAN penetrates throughout the global ocean estuarine, coastal and nearshore regions, across the area defined by the Exclusive Economic Zone (EEZ) of individual countries. The biological impacts of ALAN are likely to be more severe and widespread in regions experiencing higher values of Z_c across larger spatial scales. Z_c was calculated for each pixel as the maximum depth where underwater irradiance exceeds a predefined threshold for biologically important ALAN (E_{lim}). We define E_{lim} using the precautionary principle, following the convention set out by Davies et al. (2020). For integrated absolute irradiance measurements, E_{lim} is approximated as $0.1 \mu\text{Wm}^{-2}$, the

minimum irradiance of white light that elicits diel vertical migration in globally widespread adult *Calanus* copepods (Båtnes et al., 2015).

We confirmed the validity of our methodology using data from a field campaign in the Gulf of Aqaba, Red Sea (Tamir et al., 2017). Such datasets are extremely rare due in part to the technical difficulty of measuring multi-spectral irradiances to the level of $\mu\text{W m}^{-2} \text{nm}^{-1}$ with an associated high signal to noise ratio (SNR).

Methods

Theory

To describe the penetration and subsequent attenuation of ALAN as it propagates through the water column, Beer's Law was used for a general wavelength λ :

$$E(\lambda, z) = E_0(\lambda) \exp(-K_d(\lambda) \cdot z) \quad (\text{Equation 1})$$

where E is irradiance ($\text{W m}^{-2} \text{nm}^{-1}$), K_d the diffuse attenuation coefficient (m^{-1}) and z is depth (m).

Expanding to account for spectral wavebands, λ_i ($i = \text{blue}, \lambda_b$, nominally 400–500 nm; $i = \text{green}, \lambda_g$, nominally 500–600 nm; $i = \text{red}, \lambda_r$, nominally 600–700 nm):

$$E(z) = E_0(\lambda_b) \exp(-K_d(\lambda_b) \cdot z) + E_0(\lambda_g) \exp(-K_d(\lambda_g) \cdot z) + E_0(\lambda_r) \exp(-K_d(\lambda_r) \cdot z)$$

(Equation 2)

The left side of Equation 2 can be expanded thus:

$$E(z) = E_0 \exp(-K_d z) \quad (\text{Equation 3})$$

where the contributions of the surface irradiance in the λ_b , λ_g and λ_r are expressed as a simple sum:

$$E_0 = E_0(\lambda_b) + E_0(\lambda_g) + E_0(\lambda_r) \quad (\text{Equation 4})$$

which results in

$$[E_0(\lambda_b) + E_0(\lambda_g) + E_0(\lambda_r)] \exp(-K_d z) =$$

$$E_0(\lambda_b) \exp(-K_d(\lambda_b) \cdot z) + E_0(\lambda_g) \exp(-K_d(\lambda_g) \cdot z) + E_0(\lambda_r) \exp(-K_d(\lambda_r) \cdot z) \quad (\text{Equation 5})$$

Using spectral irradiance fractional (f) contributions to the whole

$$f_b + f_g + f_r = 1 \quad (\text{Equation 6})$$

where, e.g.:

$$f_b = \frac{E_0(\lambda_b)}{E_0(\lambda_b) + E_0(\lambda_g) + E_0(\lambda_r)} \quad (\text{Equation 7})$$

allows the relative irradiance contributions $f_{b,g,r}$ to be calculated at the surface.

Broadband (400–700 nm) K_d can be calculated using the following expression at a fixed depth (e.g., for $z = 1$ m):

$$K_d = -\ln \left[f_b \exp(-K_d(\lambda_b)) + f_g \exp(-K_d(\lambda_g)) + f_r \exp(-K_d(\lambda_r)) \right] \quad (\text{Equation 8})$$

Calculating the critical depth is then straightforward, where the irradiance drops below a preset threshold (E_{lim}):

$$Z_c = -\frac{1}{K_d} \ln \left(\frac{E_{lim}}{E_0} \right) \quad (\text{Equation 9})$$

Datasets

In order to quantify regionally and globally the amount of ALAN reaching different depths within the water column, two different datasets were used: an artificial night sky brightness world atlas (Falchi et al., 2016b) to define the above water light field; and a global dataset of in-water IOP (Sathyendranath et al., 2019b), the absorption and backscatter components being calculated using the IOP model of Lee et al. (2002). Global monthly mean climatologies (199–2017) were calculated from the primary IOP dataset (Sathyendranath et al., 2019b), specifically: the absorption due to phytoplankton at a wavelength of 443 nm, $a_{ph}(443)$; the absorption due to CDOM and particulates at 443 nm, $a_{dy}(443)$; and the backscatter due to particulates at 555 nm, $b_{bp}(555)$.

A sea-surface broadband irradiance dataset collected from Plymouth Sound and the Tamar Estuary (Davies et al., 2020) was used to convert the night sky brightness (Falchi et al., 2016b) into spectral waveband irradiances (see Modelling section). For the specification of EEZ, the global data set of the Flanders Marine Institute (2018) was used.

Modelling

The above water global artificial night sky brightness is given in units of mcd m^{-2} and is ostensibly a measure of the broadband signal. As the penetration of light through the water column has a strong spectral dependency, essentially being a function of absorption and scatter of the different optically active components (pure water, chlorophyll [phytoplankton], CDOM, suspended particulates), then the above water light field needs to be split spectrally into different bands. In this paper we use relatively wide spectral bands coincidental with the wavebands on a Skye Instruments multispectral irradiance sensor (blue, 400–500 nm; green, 495–560 nm; red, 620–740 nm) in order to empirically fit the broadband global

atlas (Falchi et al., 2016a) values to their spectral signature (Davies et al., 2020). Figure 1 shows a schematic diagram of the model framework, split into two stages.

Stage 1

A look-up-table (LUT) of spectral K_d values (blue, 400–500 nm; green, 495–560 nm; red, 620–740 nm) was generated using the HYDROLIGHT in-water radiative transfer model (Mobley, 1995) assuming a totally diffuse sky and a windspeed of 5 ms^{-1} . A four independent component model was used within HYDROLIGHT, these being: (I) pure water; (II) phytoplankton; (III) CDOM and; (IV) particles. For component I, tabulated absorption values (Smith and Baker, 1981) were used together with a pure water scattering phase function (Mobley, 1994). Components II and III are assumed to be non-scattering (i.e., no phase function required) and are described as a continuous function of wavelength. For component II, the normalized absorption coefficient data of Prieur and Sathyendranath (1981) were employed and for III, a simple exponential function was used:

$$a_{dy}(\lambda) = a_{dy}(443) \exp(-0.014(\lambda - 443)) \text{ (m}^{-1}\text{)} \quad \text{(Equation 10)}$$

Finally, component IV is assumed to be non-absorbing and is described by the spectral function for particulate backscatter (Smyth et al., 2006):

$$b_{bp}(\lambda) = b_{bp}(555) \left(\frac{\lambda}{555}\right)^{-0.5} \text{ (m}^{-1}\text{)} \quad \text{(Equation 11)}$$

together with a particle phase function (Petzold, 1972). The input IOPs to HYDROLIGHT were $a_{ph}(443)$, $a_{dy}(443)$ and $b_{bp}(555)$, based on the global IOP dataset wavelengths. Both $a_{ph}(443)$ and $a_{dy}(443)$ input values were prescribed at logarithmic intervals between 0.01 and 10.0 m^{-1} ($n = 28$), whereas $b_{bp}(555)$ ranged between 0.001 and 0.1 m^{-1} ($n = 19$) resulting in 14,896 runs of the HYDROLIGHT model for each spectral band ($\lambda_b, \lambda_g, \lambda_r$) to create a LUT. The resultant LUT was then used to calculate 12 monthly global climatology maps each of $K_d(\lambda_b, \lambda_g, \lambda_r)$ at a nominal resolution of 4 km on an equal angle projection (8192 x 4096 pixels), using a 3D weighted nearest-neighbour scheme.

Stage 2

The relationships between the global artificial night sky brightness atlas (Falchi et al., 2016b) and sea surface broadband irradiances collected from Plymouth Sound and the Tamar Estuary (Davies et al., 2020) were spectrally resolved using empirical equations of the form:

$$E_0(\lambda) = m_\lambda \times E_F + c_\lambda \text{ (}\mu\text{W m}^{-2}\text{)} \quad \text{(Equation 12)}$$

where m_λ and c_λ are the spectral slope and intercept, respectively (Table 1), and E_F is the night sky brightness (mcd m^{-2}). The c_λ term also takes into consideration the natural sky brightness as well as compensating for some of the assumptions within the Falchi et al. (2016b) atlas, such as the blue “blindness” of the Day/Night Band of the Visible Infrared Imaging Radiometer Suite (VIIRS) satellite

sensor (see section on Limitations of approach) and use of a fixed aerosol optical depth. The surface spectral light field was then propagated through the water column using a broadband formula for K_d (Equation 8), weighting each spectral band by its relative contribution to the surface irradiance (Equations 6–8). The K_d global climatological maps were resampled to match the spatial (1 km) resolution of the global artificial night sky brightness atlas. For each pixel of the regional or global map generated, determining the broadband irradiance was then possible at any given depth, or the depth below which the light levels dropped below a predetermined threshold (E_{lim}). E_{lim} was set to $0.1 \mu W m^{-2}$ based on the light sensitivity of *Calanus* (Båtnes et al., 2015), a globally widespread key diel migratory species of zooplankton important to fisheries. E_{lim} was converted from $0.47 \times 10^{-6} \mu mol \text{ photon } m^{-2} s^{-1}$ using the approximate conversion factor given by Morel and Smith (1974) for mean frequency averaged lighting conditions ($1 W m^{-2} \approx 4.6 \mu mol \text{ photons } m^{-2} s^{-1}$). The critical depth (Z_c) was calculated using Equation 9.

Validation of methodology

We used the in-water multi-spectral irradiance dataset generated on a field campaign in the Gulf of Aqaba, northern Red Sea, as reported in Tamir et al. (2017). The multi-spectral in-water light profiles were measured using a SeaWiFS-compliant, high resolution, profiling reflectance radiometer (PRR-800; Biospherical Instruments Inc., San Diego) with 19 spectral channels in the 300–900-nm wavelength range. The spectral irradiances were aggregated into 1-m depth bins, and then the entire spectrum at each depth was interpolated linearly onto a 1-nm wavelength resolution grid, which was then integrated into the broadband ranges for blue (400–500 nm), green (495–560 nm) and red (620–740 nm), for each depth and each station to allow inter-comparison to be made with the global model.

Point extractions from the global model were made at the locations of the 19 stations described in Tamir et al. (2017). These were: 1) above surface sky brightness ($mcd m^{-2}$) from the global atlas of Falchi et al. (2016a); and 2) the in-water broadband spectral $K_d(\lambda_b, \lambda_g, \lambda_r)$ extracted from the global climatological maps. The surface sky brightness was converted to the blue, green and red wavelengths ($\mu W m^{-2}$) using Equation 12 and coefficients in Table 1, and then propagated through the water column using Equation 1. This approach allowed direct inter-comparison with the in situ measured irradiances for each station as a function of depth. In addition, for each station at each 1-m depth interval, the broadband (PAR) downwelling irradiance was calculated from the three spectral components. This calculation allowed the value of Z_c to be calculated for each station.

Results

Table 2 shows the total area of individual EEZs where Z_c exceeds given depths, ranked first by the surface ($< 1 m$) component and then successively down the water column to greater depths (maximum of 50 m) for the top 20 regions. A comprehensive ranking table (Table S1) shows that around 3.1% of the world's EEZs, a total area of 1.9 million km^2 , are already impacted by ALAN. In the UK part of the North Sea

(also shown in Figure 2), ranked #5, Z_c exceeds 1 m across nearly 65,000 km², and exceeds 40 m across approximately 3000 km². Greater impacts of ALAN are anticipated at depth in EEZs with clearer waters. To give one example, the largest area where Z_c exceeds 40 m in Table 2 (4,393 km²) can be found in the Malaysian part of the South China Sea (ranked #6).

Table 3 shows the total percentage area of an individual EEZ where Z_c exceeds given depths ranked for the top 20 regions (the global ranking table is given in Table S2). Z_c exceeded 1 m across at least 60% of the surface area of all of the top 20 ranked EEZs. Seven EEZs ranked in the top 20 by percentage area in the Persian Gulf and two EEZs in the North Sea. In some of the most impacted regions (Qatari part of the Persian Gulf #4; UAE part of the Persian Gulf #9) Z_c exceeds 10 m across sizable percentages of their area (94 and 79.5% of their surface area, respectively). In these regions, extensive ALAN at the sea surface combines with clear surface waters to produce widespread impact zones at depth.

The month impacted the most by ALAN is shown in column 3 of Table 2. All regions demonstrate some form of seasonal cycle driven by blooms of phytoplankton (a function of light and nutrient availability, and water column stability) as well as riverine inputs to the marine system through suspended particulates and dissolved organic matter, or physical processes such as winter wind-driven mixing which causes significant resuspension of sediment in shallow coastal waters. From the biological impact perspective, ALAN impacts are thus likely to vary between seasons, and indeed over shorter timescales in tidally dynamic regions.

Figure 2 shows the prevalence and likely impact of ALAN on the marine environment in two of the most heavily light-polluted regions on the globe, namely the Persian Gulf and the North Sea. These regions are characterized by extensive offshore development including oil and gas platforms, windfarms and island development. The urbanized areas around the Persian Gulf fringes, such as Dubai, Abu Dhabi, Doha and Manama, as well as the North Sea fringes, such as Sunderland and Hartlepool in the UK and the extended Dutch and Belgian coastal conurbations, generally have a smaller impact on the marine ALAN field than remote offshore features of these regions. This difference is due in part to the anisotropic nature of the light pollution at the land–sea interface; i.e., a large percentage, depending on the orientation of the coastline, topography and aspect of artificial light sources, is directed inland. It is also dependent upon the clarity of the water in and around the coastal zone, governed by the IOPs, which is generally more opaque (higher K_d in Equation 9) than further offshore due to freshwater runoff from land, upwelling of nutrients and wave and tidal mixing of the water column and seabed. Water column opacity increases where sediment loading, CDOM concentrations and possibly phytoplankton densities are higher.

Figure 3 shows the inter-comparison between the global model-derived in-water light profiles and those derived from in situ measurements in the Gulf of Aqaba (Tamir et al., 2017). The purpose of including these data here is to provide quantifiable confidence in our overall methodology. The in situ multispectral measurements (Figure 3b, e, h) have been integrated to produce broadband blue, green and red irradiances to replicate our modelling (Figure 3a, d, g) approach. The logarithmic root mean square differences between the modelled and in situ data are 0.234, 0.663 and 0.634 in the blue, green and red parts of the

spectrum, respectively (Figure 3c, f, i) and replicate reasonably well the decrease in spectral irradiance with depth: less than 1% of the surface irradiances in the red penetrate below 3–5 m; around 10% of the surface green light arrives at 20 m; and more than 10% of the blue light penetrates depths deeper than 30 m in both the modelled and in situ data. The modelled Z_c (mean \pm standard deviation of 24.6 ± 1.7 m, $N = 18$) is slightly lower than the in situ observations (25.7 ± 1.3 m, $N = 18$; Station 17 removed as an obvious outlier). Important controls on the vertical light profile are the in-water IOPs: our modelled approach uses climatological monthly values (September, for the data presented) and small changes in the IOPs can have a large impact on the value of Z_c . The annual range of modelled Z_c for the stations presented here is between 21.4 ± 0.3 m ($N = 19$) in November and 24.6 ± 0.4 m ($N = 19$) in September; the average for all stations and all months is 23.5 ± 1.1 m ($N = 228$).

Discussion

Implications

Evidence for the potential impacts of ALAN across marine phylogenies and all levels of biological organization is rapidly emerging. ALAN affects multiple aspects of the life history of marine organisms, including reduced reproductive success (Witherington and Bjorndal, 1991; Fobert et al., 2019), disrupted migration (Ludvigsen et al., 2018; Berge et al., 2020; Torres et al., 2020), altered recruitment (Davies et al., 2015), and shifts in the balance of species interactions (Becker et al., 2013; Underwood et al., 2017; Levy et al., 2020). The extent of ALAN sufficient to elicit such responses in marine ecosystems is not yet known. Our atlas is the first to quantify the global spatial and temporal prevalence of biologically important ALAN in undersea habitats. It has numerous potential applications in the design of ecological experiments, biogeography and conservation.

The atlas highlights the many areas of the global ocean that are strongly impacted by ALAN from land and offshore infrastructure. ALAN penetrates to significant depths within the water column (> 40 m) depending on the clarity of the water, which itself is a function of regional biogeochemistry and season. In the most heavily light-polluted regions (Persian Gulf, Eastern Mediterranean, North Sea), there is likely significant disruption to the natural ecosystems of the region impacting every trophic level from phytoplankton upwards. The greatest direct impacts are likely on highly photosensitive species that utilize moonlight to guide migrations and synchronize phenological events (Naylor, 2001; Last et al., 2016; Ugolini et al., 2016; Ludvigsen et al., 2018; Torres et al., 2020), many of which are critical to the wider ecosystem and sustain vital ecosystem services (Moberg and Folke, 1999; Hayes, 2003).

Disruption by ALAN at the geographical scales presented here is likely to have a significant impact on an individual country's realized economic value of their EEZ. The EEZs are already regions under considerable stress from other factors such as shipping and underwater noise (Simmonds et al., 2014). This

work makes a compelling case for undersea ALAN to be included as an additional stressor within this already multi-stressed environment.

Limitations of approach

Our atlas combines remote sensing products with radiative transfer modelling to produce first insights into the exposure of undersea habitats to ALAN. The relationship between artificial sky brightness and sea surface irradiance is derived from measurements of artificial skyglow originating from the city of Plymouth, UK, recorded on clear moonless nights when the sun was $> 18^\circ$ below the horizon. Whilst the derived relationships are robust (Table 1; Figure S2 in Davies et al., 2020), our modelling approach assumes that the spectral power distribution of artificial skyglow is matched between Plymouth, a predominantly light-emitting diode (LED)-lit city, and the rest of the world. While LED lighting use is growing rapidly – forecast to contribute 97% of the global lighting market by 2025 (Bertoldi, 2018) – the modelled exposure levels may overestimate artificial light irradiances where low pressure sodium (LPS) lighting is still in use, but will remain broadly representative where other modern broad spectrum lights (for example high pressure sodium and metal halide) predominate. For an in depth study on spectral differences of artificial light sources and the differences in color between countries, see Levin et al. (2020). The *in situ* data used here and presented in Tamir et al. (2017) contained a strong peak in the sodium band (589 nm); however, the impact of this band was omitted in the modelling and the *in situ* numerical integration. We contend that this approximation is acceptable, because the absorption due to pure water (Pope and Fry, 1997) at 589 nm is around 0.135 m^{-1} , which compares with 0.009 m^{-1} (450 nm, mid-blue); 0.04 m^{-1} (530 nm, mid-green) and 0.465 m^{-1} (680 nm, mid-red). Most of the light in this sodium band will therefore be attenuated in the top few meters of the water column, and consequently contribute insignificantly to the overall broadband calculated Z_c .

The current terrestrial world atlas of Falchi et al. (2016a) uses the Day Night Band of the VIIRS satellite sensor which is “blind” in the blue part of the spectrum and cannot spectrally distinguish between sodium-based lights and the longer wavelength component of the LED emission spectrum. The outputs of our methodology could therefore be improved by new satellite missions that could spectrally quantify the ALAN signature of individual countries and urban areas.

The base dataset of the world atlas of artificial sky brightness (Falchi et al., 2016a) is limited to clear sky conditions, hence so are the values of underwater irradiance we present here. Cloud cover and cloud base height can amplify light pollution (Davies et al., 2020) by an order of magnitude in luminance (Kyba et al., 2011). The reported exposure irradiances and values of Z_c will therefore be higher when clouds are present. However, this effect may be offset by the clouds, particularly when there is a low altitude cloud base, rapidly attenuating the upward propagation of the surface light field and limiting the far field effects of ALAN. The near-field effects of individual street lights, although considerable on scales $< 10 \text{ m}$, rapidly decrease with distance and, when interacting with the aquatic environment, much of the light is reflected at

the surface (Jechow and Hölker, 2019); the far-field skyglow term will tend to dominate the in-water impacts at distances > 100 m as point sources appear closer to the horizon.

The coverage from ocean color satellites used to generate the in-water IOP fields does not include high latitudes ($> 50^\circ$) during the winter months (boreal, December–February; austral, June–August). This limitation is of most relevance in the northern hemisphere, as there are few population centers poleward of 50°S .

The $0.1 \mu\text{Wm}^{-2}$ value for E_{lim} was selected based on the importance to fisheries of globally pervasive diel migratory species such as *Calanus*. However, other values of E_{lim} could have been chosen and alternative values are listed extensively elsewhere (Davies and Smyth, 2018; Tidau et al., 2021). Figure 4 of Davies and Smyth (2018) plots the light sensitivity of several different marine invertebrates as a function of light penetration depth. When comparing the sensitivity to types of light source (artificial skyglow and point source) and in-water optical properties, *Calanus* is shown to be particularly sensitive, which in turn relates to deeper values of Z_c . As not all sensitivity thresholds can be accommodated in any one system, even if available, we adopted a precautionary approach in using the most sensitive species. The value of E_{lim} also depends upon assuming the mean frequency of averaged lighting conditions which changes depending upon the light source itself (e.g., daylight or artificial light). McCree (1981) showed that assuming this mean frequency gives a variation of around $\pm 8.5\%$.

By using monthly climatologies of IOPs to modulate the ALAN field through the water column, our atlas adds novel insight into temporal variability and hence seasonal impacts of ALAN. This higher temporal resolution in our approach is limited by a lack of similar temporal resolution in the above surface ALAN. For long-term studies (multi-annual to decadal) as urbanization accelerates and the spectral signatures inevitably shift, changes to the above surface ALAN are likely to become increasingly important. Again, improvements in tools to quantify above sea surface ALAN levels will improve our understanding of ALAN impacts underwater.

The ocean colour sensors used to derive IOPs as part of the Climate Change Initiative dataset (Sathyendranath et al., 2019a) measure top-of-the-atmosphere radiances. These measurements are then used to derive water-leaving radiances, $L_w(\lambda)$, which involves use of an atmospheric correction procedure (Steinmetz et al., 2011): typically the atmospheric signal contributes 80% or more to the top of the atmosphere radiances (Müller et al., 2015). $L_w(\lambda)$ in turn is controlled by the in-water IOPs of absorption, $a(\lambda)$, and back-scattering, $b_b(\lambda)$. The Lee et al. (2002) IOP model used to invert $L_w(\lambda)$ into $a_{\text{ph}}(443)$, $a_{\text{dy}}(443)$ and $b_{\text{bp}}(555)$ employed a quasi-analytical algorithm which sought to limit the amount of empirical relationships contained within its framework. This approach minimises any likely errors caused by region-specific datasets used to derive IOP relationships and also makes the algorithm more generally applicable to coastal (Case 2) as well as open-ocean (Case 1) waters (Morel and Prieur, 1977). We therefore sought to minimise any limitations in the IOP dataset by using products that utilise algorithms suited to atmospheric correction (Steinmetz et al., 2011) and IOP retrieval (Lee et al., 2002) in the regions close to shore.

Management/policy implementation

In theory, the amelioration of ALAN impacts upon marine, and indeed terrestrial, ecosystems could be achieved instantly: simply turning off the lights at night would have an immediate effect. Such immediacy contrasts starkly with the multifaceted challenges posed by anthropogenic emissions of greenhouse gases into the atmosphere, which typically have decadal to centennial residence times and are intimately linked to global economic growth and prosperity. However, achieving a direct response is highly unlikely and runs counter to the observed trend towards increased use of artificial light in urban areas due to various other societal concerns. A staged approach to limiting ALAN is therefore more realistic and pragmatic, particularly as many regions of the world have only recently adopted LED technology to replace older LPS lighting. LED lighting peaks more strongly in the blue end of the spectrum, compared with the orange–red of LPS, and penetrates deeper into the water column by virtue of the optical properties of pure water (Pope and Fry, 1997; Smith and Baker, 1981). This deeper penetration is offset somewhat in more productive coastal and estuarine waters where contributions to absorption by phytoplankton and CDOM (Prieur and Sathyendranath, 1981) become significant in the blue. However, even in these more optically complex inshore waters, blue and green light originating from ALAN penetrates much further into the water column than red (Davies et al., 2020). Therefore, rather than the Spartan approach to coastal urban lighting of turning everything off at night, likely solutions could employ some form of filtering or spectral tuning of the LED lighting (i.e., low Kelvin) in order to offset some of the worst impacts.

Conclusion

We have calculated the critical depth (Z_c) to which biologically detectable light can penetrate the water column for the global coastal ocean, as represented by Exclusive Economic Zones. We have quantified the regions of the global coastal ocean which are already heavily impacted by ALAN, namely areas characterized by widespread offshore developments as well as large coastal urban areas. The global transition towards white LED lighting will likely exacerbate in-water light pollution and its impact across species, populations and marine ecosystems. This atlas on global marine light pollution can provide a powerful tool to guide research and conservation to mitigate the ecological impacts of ALAN.

References

- Båtnes, AS, Miljeteig, C, Berge, J, Greenacre, M, Johnsen, G. 2015. Quantifying the light sensitivity of *Calanus* spp. during the polar night: potential for orchestrated migrations conducted by ambient light from the sun, moon, or aurora borealis? *Polar Biology* **38**(1): 51–65. doi:10.1007/s00300-013-1415-4.
- Becker, A, Whitfield, AK, Cowley, PD, Järnegren, J, Næsje, TF. 2013. Potential effects of artificial light associated with anthropogenic infrastructure on the abundance and foraging behaviour of estuary-associated fishes. *Journal of Applied Ecology* **50**: 43–50. doi:10.1111/1365-2664.12024.

- Bennie, J, Davies ,TW, Duffy, JP, Inger, R, Gaston, KJ. 2014. Contrasting trends in light pollution across Europe based on satellite observed night time lights. *Scientific Reports* **4**(1): 3789. doi:10.1038/srep03789.
- Berge, J, Geoffroy, M, Daase, M, Cottier, F, Priou, P, Cohen, JH, Johnsen, G, McKee, D, Kostakis, I, Renaud, PE, Vogedes, D, Anderson, P, Last, KS, Gauthier, S. 2020. Artificial light during the polar night disrupts Arctic fish and zooplankton behaviour down to 200 m depth. *Communications Biology* **3**(1): 102. doi:10.1038/s42003-020-0807-6.
- Bertoldi, G. 2018. *Status of LED-Lighting world market in 2017*. Ispra: European Commission.
- Davies, TW, Coleman, M, Griffith, KM, Jenkins, SR. 2015. Night-time lighting alters the composition of marine epifaunal communities. *Biology Letters* **11**(4): 20150080. doi:10.1098/rsbl.2015.0080.
- Davies, TW, Duffy, JP, Bennie, J, Gaston, KJ. 2014. The nature, extent, and ecological implications of marine light pollution. *Frontiers in Ecology and the Environment* **12**(6): 347–355.
- Davies TW, McKee D, Fishwick J, Tidau S, Smyth T. 2020. Biologically important artificial light at night on the seafloor. *Scientific Reports* **10**(1): 12545. doi:10.1038/s41598-020-69461-6.
- Davies, TW, Smyth, T. 2018. Why artificial light at night should be a focus for global change research in the 21st century. *Global Change Biology* **24**(3): 872–882. doi:<https://doi.org/10.1111/gcb.13927>.
- Duffy, JP, Bennie, J, Durán ,AP, Gaston, KJ. 2015. Mammalian ranges are experiencing erosion of natural darkness. *Scientific Reports* **5**: 12042–12042. doi:10.1038/srep12042.
- Falchi ,F, Cinzano, P, Duriscoe, D, Kyba, CCM, Elvidge, CD, Baugh, K, Portnov, BA, Rybnikova, NA, Furgoni, R. 2016a. The new world atlas of artificial night sky brightness. *Science Advances* **2**(6): e1600377. doi:10.1126/sciadv.1600377.
- Falchi, F, Cinzano, P, Duriscoe, D, Kyba, CCM, Elvidge, CD, Baugh, K, Portnov, B, Rybnikova, NA, Furgoni, R. 2016b. Supplement to: The new world atlas of artificial night sky brightness. GFZ Data Services. <http://doi.org/10.5880/GFZ.1.4.2016.001>.
- Flanders Marine Institute. 2018. The intersect of the Exclusive Economic Zones and IHO sea areas, version 3. doi:10.14284/324 [dataset]. Flanders Marine Institute. Available at <http://www.marineregions.org/>.
- Fobert, EK, Burke da Silva, K, Swearer, SE. 2019. Artificial light at night causes reproductive failure in clownfish. *Biology Letters* **15**(7): 20190272. doi:10.1098/rsbl.2019.0272.
- Gaston, KJ, Duffy, JP, Bennie, J. 2015. Quantifying the erosion of natural darkness in the global protected area system. *Conservation Biology* **29**(4): 1132–1141. doi:10.1111/cobi.12462.
- Hayes, GC. 2003. A review of the adaptive significance and ecosystem consequences of zooplankton diel vertical migrations. *Hydrobiologia* **503**: 163–170.
- Jechow, A, Hölker, F. 2019. How dark is a river? Artificial light at night in aquatic systems and the need for comprehensive night-time light measurements. *WIREs Water* **6**(6): e1388. doi:<https://doi.org/10.1002/wat2.1388>.
- Kupprat, F, Holker, F, Kloas, W. 2020. Can skyglow reduce nocturnal melatonin concentrations in Eurasian perch? *Environmental Pollution* **262**. doi:10.1016/j.envpol.2020.114324.
- Kyba, CCM, Kuester, T, De Miguel, AS, Baugh, K, Jechow, A, Hölker, F, Bennie, J, Elvidge, CD, Gaston, KJ, Guanter, L. 2017. Artificially lit surface of Earth at night increasing in radiance and extent. *Science Advances* **3**(11): 1–9. doi:10.1126/sciadv.1701528.
- Kyba, CCM, Ruhtz, T, Fischer, J, Holker, F. 2011. Cloud coverage acts as an amplifier for ecological light pollution in urban ecosystems. *Plos One* **6**(3). doi:10.1371/journal.pone.0017307.

- Last, KS, Hobbs, L, Berge, J, Brierley, AS, Cottier, F. 2016. Moonlight drives ocean-scale mass vertical migration of zooplankton during the Arctic winter. *Current Biology* **26**(2): 244–251. doi:10.1016/j.cub.2015.11.038.
- Lee, ZP, Carder, KL, Arnone, RA. 2002. Deriving inherent optical properties from water color: a multiband quasi-analytical algorithm for optically deep waters. *Applied Optics* **41**: 5755–5772.
- Levin, N, Kyba, CCM, Zhang, QL, de Miguel, AS, Roman, MO, Li, X, Portnov, BA, Molthan, AL, Jechow, A, Miller, SD, Wang, Z, Shrestha, RM, Elvidge, CD. 2020. Remote sensing of night lights: A review and an outlook for the future. *Remote Sensing of Environment* **237**. doi:10.1016/j.rse.2019.111443.
- Levy, O, de Barros Marangoni, LF, Benichou, JIC, Rottier, C, Béraud, E, Grover, R, Ferrier-Pagès, C. 2020. Artificial light at night (ALAN) alters the physiology and biochemistry of symbiotic reef building corals. *Environmental Pollution* **266**: 114987. doi:<https://doi.org/10.1016/j.envpol.2020.114987>.
- Ludvigsen, M, Berge, J, Geoffroy, M, Cohen, JH, De La Torre, PR, Nornes, SM, Singh, H, Sørensen, AJ, Daase, M, Johnsen, G. 2018. Use of an autonomous surface vehicle reveals small-scale diel vertical migrations of zooplankton and susceptibility to light pollution under low solar irradiance. *Science Advances* **4**(1): 1–9. doi:10.1126/sciadv.aap9887.
- Mazor, T, Levin, N, Possingham, HP, Levy, Y, Rocchini, D, Richardson, AJ, Kark, S. 2013. Can satellite-based night lights be used for conservation? The case of nesting sea turtles in the Mediterranean. *Biological Conservation* **159**(0): 63–72. doi:<http://dx.doi.org/10.1016/j.biocon.2012.11.004>.
- McCree, KJ. 1981. Photosynthetically active radiation, in Lang OL, Novel P, Osmond B, Ziegler H eds., *Physiological plant ecology*. Berlin, Heidelberg, New York: Springer-Verlag.
- McLaren, JD, Buler, JJ, Schreckengost, T, Smolinsky, JA, Boone, M, Emiel van Loon, E, Dawson, DK, Walters, EL. 2018. Artificial light at night confounds broad-scale habitat use by migrating birds. *Ecology Letters* **21**(3): 356–364. doi:10.1111/ele.12902.
- Moberg, F, Folke, C. 1999. Ecological goods and services of coral reef ecosystems. *Ecological Economics* **29**(2): 215–233. doi:[http://dx.doi.org/10.1016/S0921-8009\(99\)00009-9](http://dx.doi.org/10.1016/S0921-8009(99)00009-9).
- Mobley, CD. 1994. *Light and Water; Radiative Transfer in Natural Waters*. San Diego, Calif.: Academic.
- Mobley, CD. 1995. HYDROLIGHT 3.0 User's Guide. Menlo Park, Calif.
- Morel, A, Prieur, L. 1977. Analysis of variations in ocean color. *Limnology and Oceanography* **22**(4): 709–722. doi:10.4319/lo.1977.22.4.0709.
- Morel, A, Smith, RC. 1974. Relation between total quanta and total energy for aquatic photosynthesis. *Limnology and Oceanography* **19**(4): 591–600. doi:10.4319/lo.1974.19.4.0591.
- Müller, D, Krasemann, H, Brewin, RJW, Brockmann, C, Deschamps, P-Y, Doerffer, R, Fomferra, N, Franz, BA, Grant, MG, Groom, SB, Mélin, F, Platt, T, Regner, P, Sathyendranath, S, Steinmetz, F, Swinton, J. 2015. The Ocean Colour Climate Change Initiative: I. A methodology for assessing atmospheric correction processors based on in-situ measurements. *Remote Sensing of Environment* **162**: 242–256. doi:<https://doi.org/10.1016/j.rse.2013.11.026>.
- Naylor, E. 2001. Marine animal behaviour in relation to lunar phase. *Earth Moon and Planets* **85–86**: 291–302.
- Neumann, B, Vafeidis, AT, Zimmermann, J, Nicholls, RJ. 2015. Future coastal population growth and exposure to sea-level rise and coastal flooding – a global assessment. *PLoS One* **10**(6): e0131375. doi:10.1371/journal.pone.0131375.
- Petzold, TJ. 1972. Volume scattering functions for selected natural waters. Visibility Laboratory, San Diego, CA, SIO: Scripps Institution of Oceanography.

- Pope, RM, Fry, ES. 1997. Absorption spectrum (380–700 nm) of pure water. II. Integrating cavity measurements. *Applied Optics* **36**: 8710–8722.
- Prieur, L, Sathyendranath, S. 1981. An optical classification of coastal and oceanic waters based on the specific spectral absorption curves of phytoplankton pigments, dissolved organic matter, and other particulate materials. *Limnology and Oceanography* **26**: 671–689.
- Sathyendranath, S, Brewin, RJW, Brockmann, C, Brotas, V, Calton, B, Chuprin, A, Cipollini, P, Couto, AB, Dingle, J, Doerffer, R, Donlon, C, Dowell, M, Farman, A, Grant, M, Groom, S, Horseman, A, Jackson, T, Krasemann, H, Lavender, S, Martinez-Vicente, V, Mazeran, C, Melin, F, Moore, TS, Muller, D, Regner, P, Roy, S, Steele, CJ, Steinmetz, F, Swinton, J, Taberner, M, Thompson, A, Valente, A, Zühlke, M, Brando, VE, Feng, H, Feldman, G, Franz, BA, Frouin, R, Gould, RW, Hooker, SB, Kahru, M, Kratzer, S, Mitchell, BG, Muller-Karger, FE, Sosik, HM, Voss, KJ, Werdell, J, Platt, T. 2019a. An ocean-colour time series for use in climate studies: the experience of the Ocean-Colour Climate Change Initiative (OC-CCI). *Sensors* **19**(19). doi:10.3390/s19194285.
- Sathyendranath, S, Jackson, T, Brockmann, C, Brotas, V, Calton, B, Chuprin, A, Clements, O, Cipollini, P, Danne, O, Dingle, J, Donlon, C, Grant, M, Groom, S, Krasemann, H, Lavender, S, Mazeran, C, Mélin, F, Moore, TS, Müller, D, Regner, P, Steinmetz, F, Steele, C, Swinton, J, Valente, A, Zühlke, M, Feldman, G, Franz, B, Frouin, R, Werdell, J, Platt, T. 2019b. ESA Ocean Colour Climate Change Initiative (Ocean_Colour_cci): Version 4.0 Data. Centre for Environmental Data Analysis. doi:10.5285/00b5fc99f9384782976a4453b0148f49.
- Simmonds, MP, Dolman, SJ, Jasny, M, Parsons, ECM, Weilgart, L, Wright, AJ, Leaper, R. 2014. Marine noise pollution – increasing recognition but need for more practical action. *Journal of Ocean Technology* **9**(1): 71–90.
- Smith, RC, Baker, KS. 1981. Optical properties of the clearest natural waters (200–800 nm). *Applied Optics* **20**: 177–184.
- Smyth, TJ, Moore, GF, Hirata, T, Aiken, J. 2006. Semianalytical model for the derivation of ocean color inherent optical properties: description, implementation, and performance assessment. *Applied Optics* **45**: 8116–8131.
- Steinmetz, F, Deschamps, P-Y, Ramon, D. 2011. Atmospheric correction in presence of sun glint: application to MERIS. *Opt Express* **19**(10): 9783–9800. doi:10.1364/OE.19.009783.
- Tamir, R, Lerner, A, Haspel, C, Dubinsky, Z, Iluz, D. 2017. The spectral and spatial distribution of light pollution in the waters of the northern Gulf of Aqaba (Eilat). *Scientific Reports* **7**: 42329–42329. doi:10.1038/srep42329.
- Tidau, S, Smyth, T, McKee, D, Wiedenmann, J, D’Angelo, C, Wilcockson, D, Ellison, A, Grimmer, AJ, Jenkins, SR, Widdicombe, S, Queirós, AM, Talbot, E, Wright, A, Davies, TW. 2021. Marine artificial light at night: An empirical and technical guide. *Methods in Ecology and Evolution* **12**(9): 1588–1601. doi:<https://doi.org/10.1111/2041-210X.13653>.
- Torres, D, Tidau, S, Jenkins, S, Davies, T. 2020. Artificial skyglow disrupts celestial migration at night. *Current Biology* **30**(12): R696–R697. doi:10.1016/j.cub.2020.05.002.
- Ugolini, A, Hoelters, LS, Ciofini, A, Pasquali, V, Wilcockson, DC. 2016. Evidence for discrete solar and lunar orientation mechanisms in the beach amphipod, *Talitrus saltator* Montagu (Crustacea, Amphipoda). *Scientific Reports* **6**: 1–8. doi:10.1038/srep35575.
- Underwood, CN, Davies, TW, Queirós, AM. 2017. Artificial light at night alters trophic interactions of intertidal invertebrates. *Journal of Animal Ecology* **86**(4): 781–789. doi:10.1111/1365-2656.12670.
- West, G. 2018. *Scale: The universal laws of life and death in organisms, cities and companies*. London: Weidenfield & Nicholson.

Witherington, BE, Bjorndal, KA. 1991. Influences of artificial lighting on the seaward orientation of hatchling loggerhead turtles *Caretta caretta*. *Biological Conservation* **55**(2): 139–149. doi:10.1016/0006-3207(91)90053-C.

Contributions

Contributed to conception and design: TS, TD, AW

Contributed to acquisition of data: TS, TD, DM, RT, ZD, DI

Contributed to analysis and interpretation of data: TS, TD, AW

Drafted and/or revised the article: TS, AW, TD, ST, DM, RT, ZD, DI

Approved the submitted version for publication: TS, AW, TD, ST, DM, RT, ZD, DI

Acknowledgments

The authors would like to thank Fabio Falchi for making the entire floating-point dataset from the 2016 World Atlas of Artificial Night Sky Brightness available to us upon request.

Funding information

UK Natural Environment Research Council grant NE/S003568/1 (TS, TD, DM, AW, ST). Israel Ministry of Science, Technology, and Space, Office of Energy and Water, grant number 3-11110 (RT, DI, ZD).

Competing interests

The authors have declared that no competing interests exist.

Supplemental material

- **Figures:** 11 figures (S1–S11) appended to the end of this document
- **All Global EEZ ALAN impact dataset:** Excel File, containing Tables S1 and S2.
 - **Filename:** “Supplementary Materials - EEZ ALAN impact ranking tables.xlsx”

Data accessibility statement

Global fields of Z_c in netCDF format can be accessed from

<https://doi.pangaea.de/10.1594/PANGAEA.929749>. Code used to create the global fields can be accessed

via <https://github.com/timjsmyth/ALAN>.

Figures

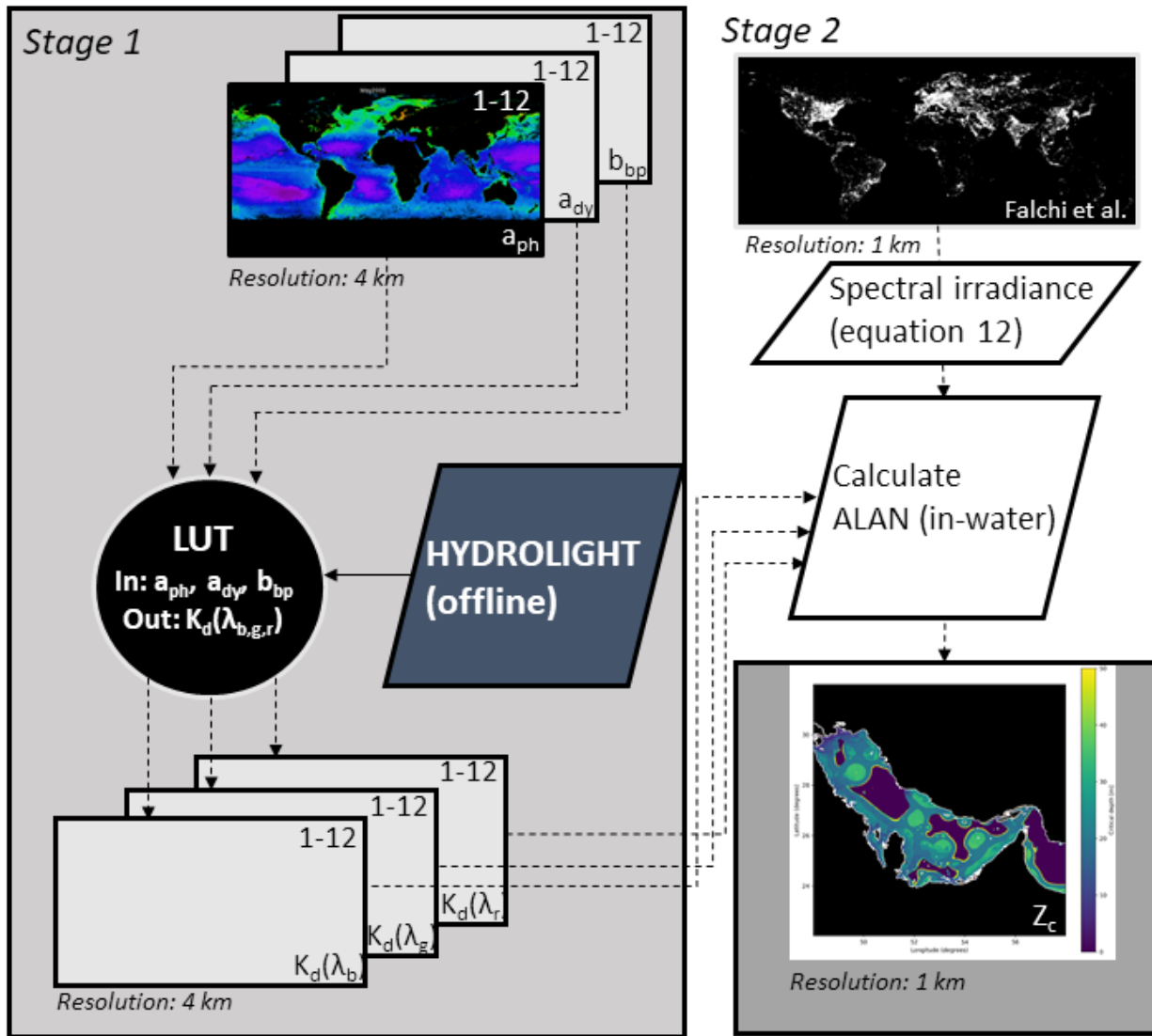


Figure 1. Schematic of the modelling approach. In Stage 1, the spectrally resolved values of the (in-water) diffuse attenuation coefficient (K_d) are calculated based on offline runs of a hydro-optical model (HYDROLIGHT) used to create a look-up-table (LUT). Inputs are monthly climatologies (1–12) of global inherent optical property fields: phytoplankton absorption (a_{ph}); coloured dissolved organic matter absorption (a_{dy}); and particulate backscattering (b_{bp}). In Stage 2, a combination of the Falchi et al. (2016a) ALAN atlas converted to above water spectral irradiance (using empirical Equation 12) and the K_d fields is used to calculate the critical depth (Z_c ; Equation 9).

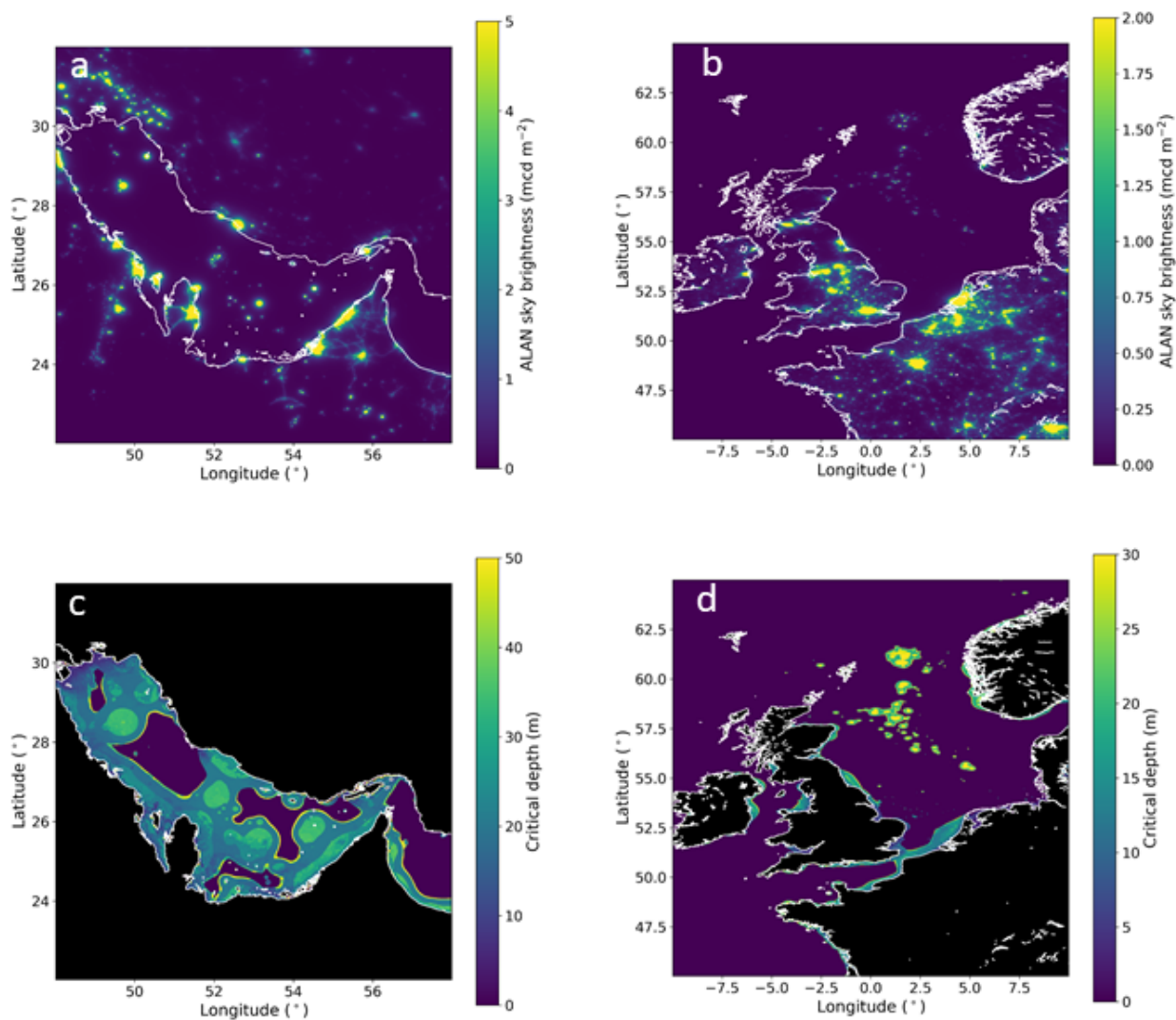


Figure 2. Sky brightness and in-water critical depth. ALAN sky brightness from the global atlas of Falchi et al. (2016a) for the (a) Persian Gulf and (b) North Sea, two of the most ALAN-polluted regions on the globe (Table 2). In-water impact of ALAN shown as the critical depth (Z_c) parameter for the (c) Persian Gulf and (d) North Sea. Note different scales for ALAN and Z_c between the two regions.

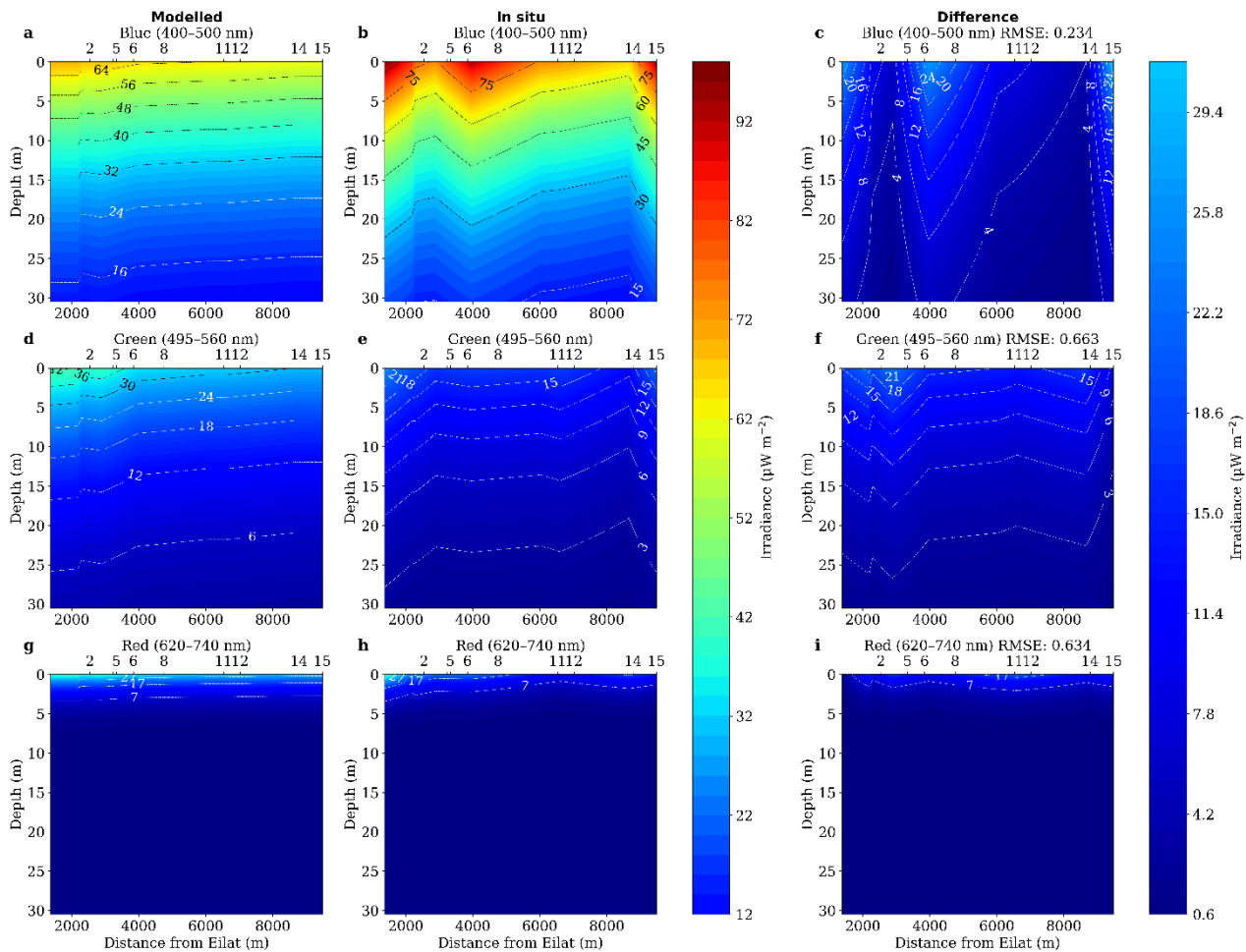


Figure 3. Comparison between modelled and in situ in-water irradiances ($\mu\text{W m}^{-2}$). For station locations within the Gulf of Aqaba (see original data in Tamir et al., 2017): station number on the top x-axis, station distance (m) away from the centre of Eilat (29.56°N , 34.95°E) on the bottom x-axis. Blue (400–500 nm) integrated irradiances for a) modelled b) in situ and associated c) difference, with root mean squared difference (RMSD); green (495–560 nm) integrated irradiances for d) modelled e) in situ and associated f) difference; and red (620–740 nm) integrated irradiance for g) modelled h) in situ and associated i) difference, all as a function of distance (x-axis) and depth (y-axis).

Tables

Table 1. Relationships between artificial night sky brightness (mcd m^{-2}) and spectral irradiance ($\mu\text{W m}^{-2}$) for clear skies (Davies et al., 2020)

$E_0 (\lambda)$	m^a	c	pseudo F^b	p^b
Blue (400–500 nm)	4.53	59.58	12.2	< 0.01
Green (495–560 nm)	7.27	25.09	16.4	< 0.001
Red (620–740 nm)	6.37	26.20	25.9	< 0.001

^a Fitted using a quantile regression on the median to reduce leverage of measurements taken directly under artificial light sources, which are not representative of sky brightness.

^aDerived from Wald tests

Table 2. EEZ area (km²) affected by ALAN ranked by area affected just below the sea surface (1 m)

Rank	EEZ Long Descriptor	Month most impacted	Total area (km ²)	Total area (km ²) affected by ALAN > Z (m)				
				> 1	> 10	> 20	> 30	> 40
1	Iranian part of the Persian Gulf	Dec	119,714	71,589	68,716	24,781	3,951	359
2	South Korean part of the Japan Sea	Apr	222,288	66,242	64,908	39,567	20,006	2,223
3	Vietnamese part of the South China Sea	Dec	785,201	65,172	62,816	21,200	10,993	3,926
4	Chinese part of the Yellow Sea	Oct	342,731	65,119	19,536	1,714	685	343
5	United Kingdom part of the North Sea	Apr	489,021	65,040	54,281	25,918	12,715	2,934
6	Malaysian part of the South China Sea	Dec	439,335	52,281	51,402	41,737	19,331	4,393
7	Chinese part of the South China Sea	Dec	518,534	49,261	36,297	10,371	3,111	1,037
8	Japanese part of the Japan Sea	Apr	708,092	46,026	46,026	32,572	14,870	2,124
9	Nigerian part of the Gulf of Guinea	Oct	190,972	43,924	39,149	21,771	8,212	955
10	United Arab Emirates part of the Persian Gulf	Nov	53,317	42,494	42,387	18,714	4,159	1,386
11	Chinese part of the Eastern China Sea	Sep	342,463	41,780	5,822	1,370	685	342
12	Italian part of the Adriatic Sea	Dec	87,988	35,547	34,667	11,438	3,520	792
13	Thailand part of the Gulf of Thailand	Dec	193,725	33,708	33,321	23,247	8,718	1,550
14	Italian part of the Tyrrhenian Sea	Dec	297,085	32,976	32,976	29,411	5,942	1,188
15	Finnish part of the Gulf of Bothnia	May	145,359	32,706	11,047	1,163	436	145
16	Mexican part of the Gulf of Mexico	Dec	887,462	31,949	30,174	16,862	9,762	887

17	Qatari part of the Persian Gulf	Jan	33,786	31,793	31,759	12,636	1,250	68
18	Algerian part of the Mediterranean Sea - Western Basin	Dec	166,920	30,046	30,046	27,041	8,847	334
19	Saudi Arabian part of the Persian Gulf	Nov	37,437	29,987	29,538	7,562	973	524
20	Angolan part of the South Atlantic Ocean	Feb	447,840	29,557	28,214	6,270	896	448
- ^a	Global totals	-	61,679,477	1,918,367	1,641,569	838,054	290,614	91,619

^aNot applicable

Table 3. EEZ area affected by ALAN ranked by percentage impacted just below the sea-surface (1 m)

Rank	EEZ Long Descriptor	Month most impacted	Total area (km ²)	Percentage (%) of region affected by ALAN > Z (m)				
				> 1	> 10	> 20	> 30	> 40
1	Iraqi part of the Persian Gulf	Apr	940	100	30.6	4.5	4.5	0.2
2	Overlapping claim Palestinian part of the Mediterranean Sea	Dec	600	99.8	99.8	99.8	68.8	34.2
3	French part of the North Sea	Oct	2,372	98.6	97.8	3.6	0.1	0
4	Qatari part of the Persian Gulf	Jan	33,786	94.1	94	37.4	3.7	0.2
5	Turkish part of the Sea of Marmara	Dec	14,378	93	90.9	15.3	1.8	0.2
6	Bahraini part of the Persian Gulf	Nov	8,885	83.2	82.1	30.3	3.9	1.7
7	Belgian part of the North Sea	Sep	4,245	80.2	70.1	7.5	0	0
8	Saudi Arabian part of the Persian Gulf	Nov	37,437	80.1	78.9	20.2	2.6	1.4
9	United Arab Emirates part of the Persian Gulf	Nov	53,317	79.7	79.5	35.1	7.8	2.6
10	Overlapping claim Gibraltarian part of the Alboran Sea	Dec	148	79.1	78.4	68.9	41.2	2.7
11	United Arab Emirates part of the Gulf of Oman	Mar	4,580	76.7	76.6	34.2	11	2.2
12	US Southeast Alaska and British Columbia	Jan	7,508	76.3	69.6	5.4	1.9	0.7
13	Kuwaiti part of the Persian Gulf	Feb	12,993	74.9	61.3	12	2.7	1.6
14	Egyptian part of the Gulf of Suez	Dec	10,692	70.5	70.5	59.4	24.3	2.4

15	Japanese part of the Seto Naikai	Dec	16,756	65.7	65.1	9	4.1	0.5
16	Spanish part of the Strait of Gibraltar	Nov	619	62.4	61.4	47.7	13.1	4.8
17	Iran / UAE part of the Persian Gulf	Nov	5,872	60	60	13	6.8	0.1
18	Moroccan part of the Strait of Gibraltar	Dec	810	59.9	59.1	46.8	30.9	2.2
19	Iranian part of the Persian Gulf	Dec	119,714	59.8	57.4	20.7	3.3	0.3
20	Swedish part of the Kattegat	Feb	12,334	59.8	30.5	1.1	0.1	0.0
-	Global totals	-	-	3.11	2.66	1.36	0.47	0.15

^aNot applicable

Supplemental material

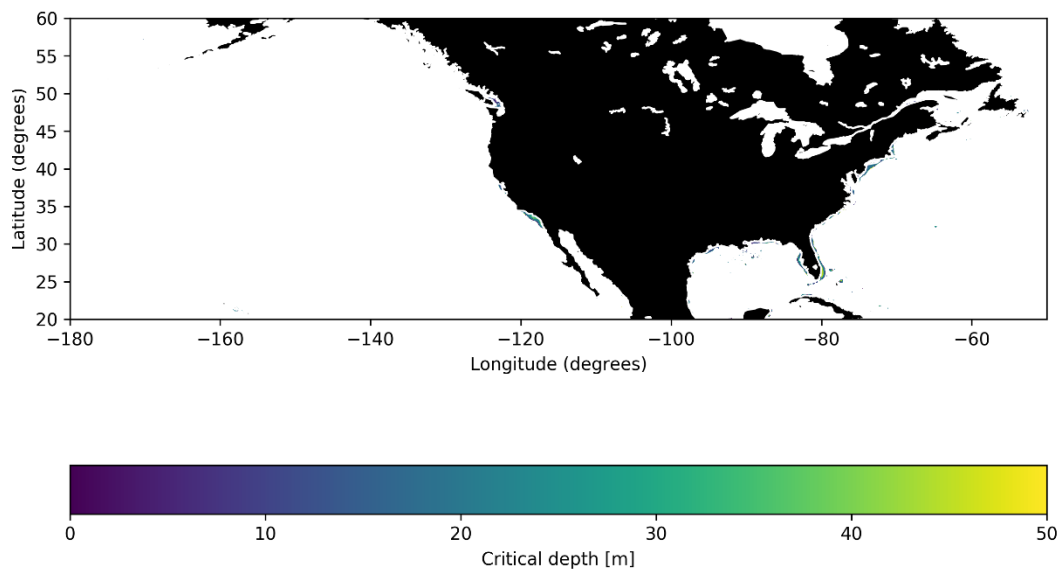


Figure S1. Critical depth (Z_c) for climatological May for North America. Entire dataset can be downloaded in netCDF format from Pangaea (<https://doi.pangaea.de/10.1594/PANGAEA.929749>)

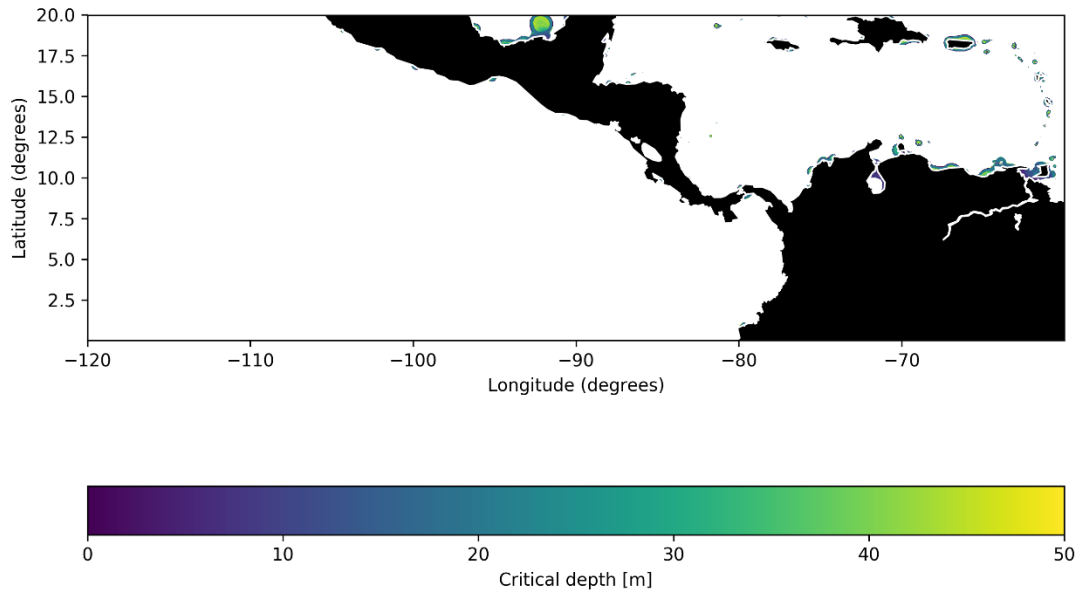


Figure S2. Critical depth (Z_c) for climatological May for Central America. Entire dataset can be downloaded in netCDF format from Pangaea (<https://doi.pangaea.de/10.1594/PANGAEA.929749>)

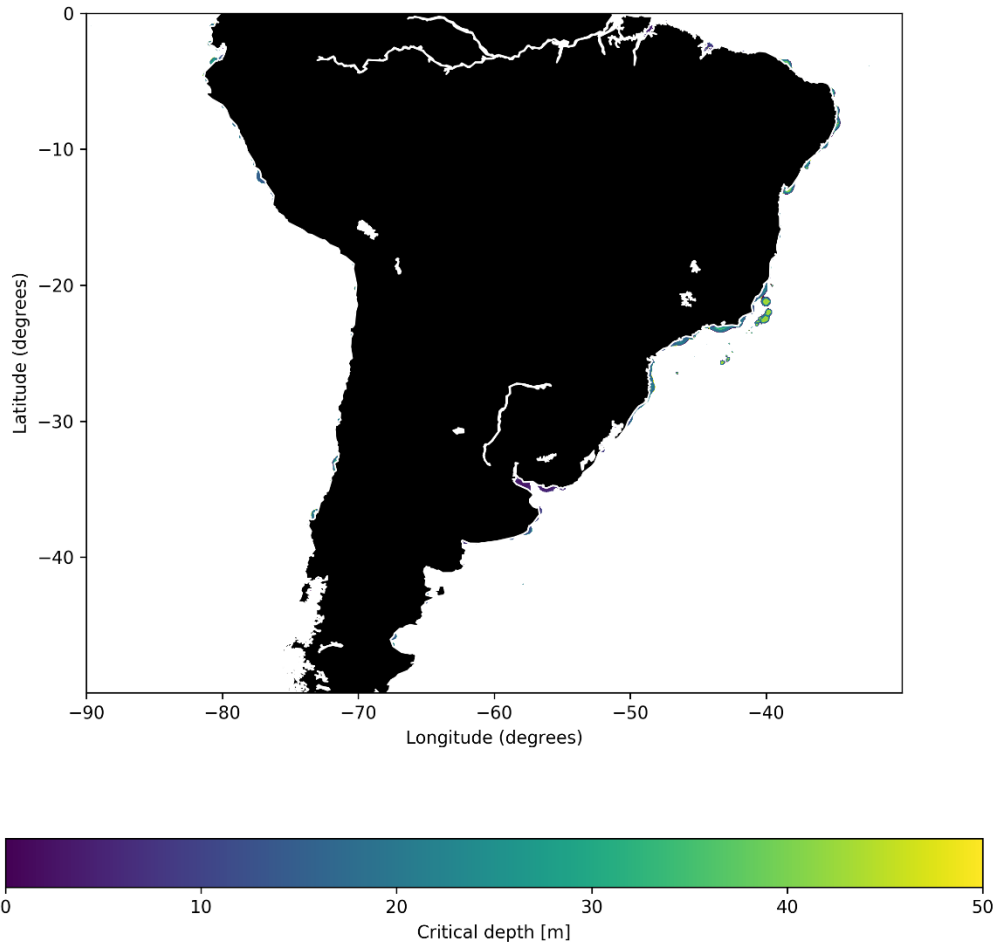


Figure S3. Critical depth (Z_c) for climatological May for South America. Entire dataset can be downloaded in netCDF format from Pangaea (<https://doi.pangaea.de/10.1594/PANGAEA.929749>).

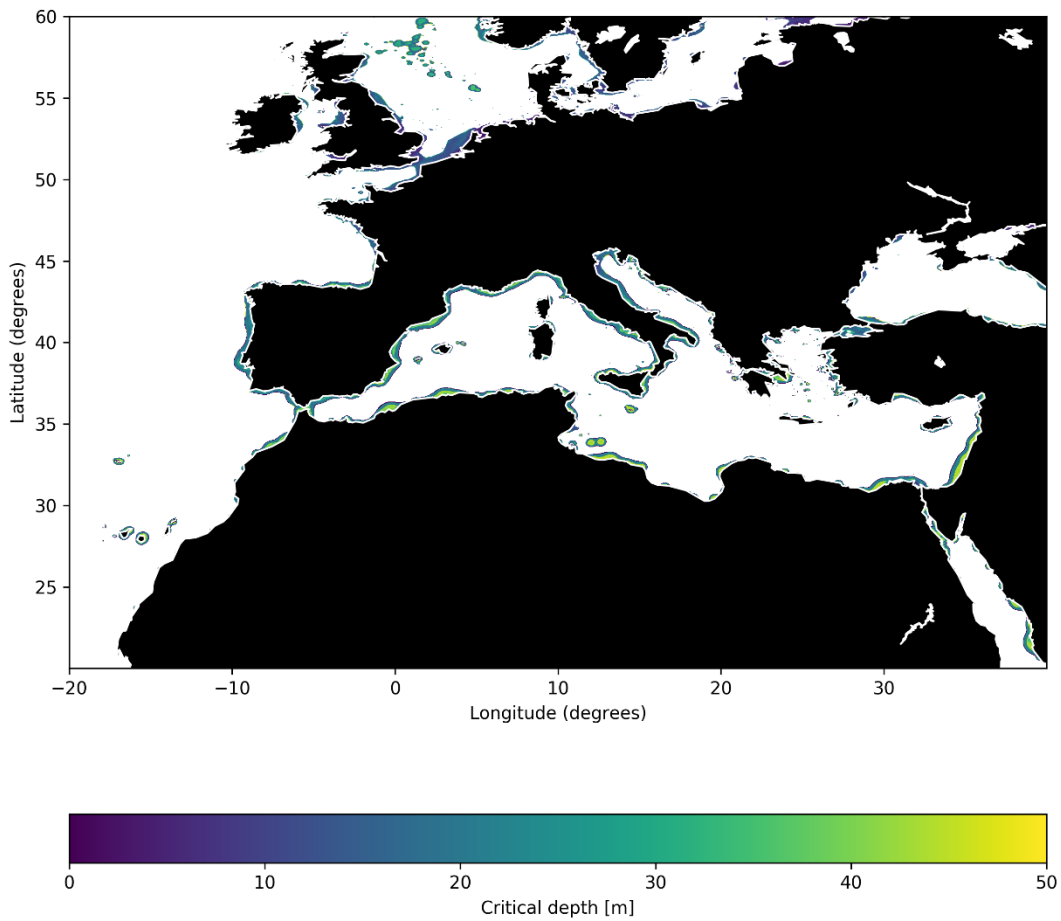


Figure S4. Critical depth (Z_c) for climatological May for Europe, Northern Africa and Mediterranean. Entire dataset can be downloaded in netCDF format from Pangaea (<https://doi.pangaea.de/10.1594/PANGAEA.929749>).

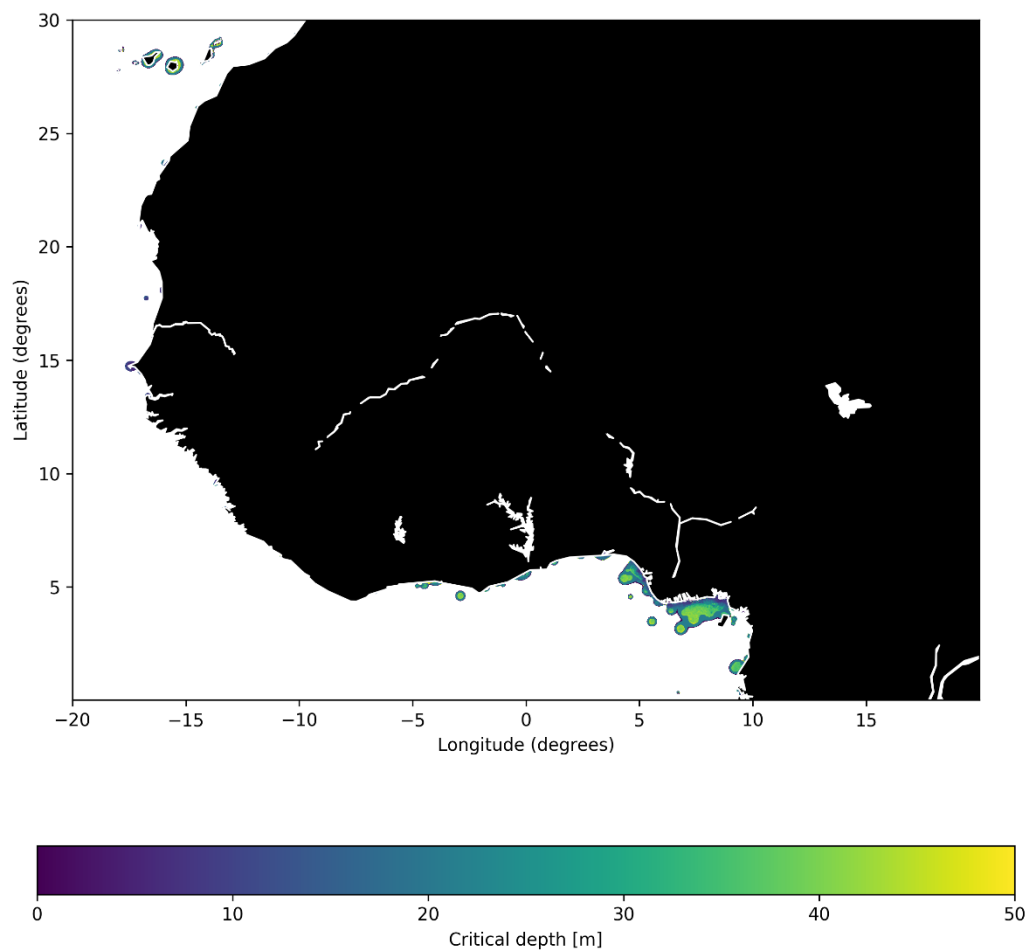


Figure S5. Critical depth (Z_c) for climatological May for northwest Africa. Entire dataset can be downloaded in netCDF format from Pangaea (<https://doi.pangaea.de/10.1594/PANGAEA.929749>).

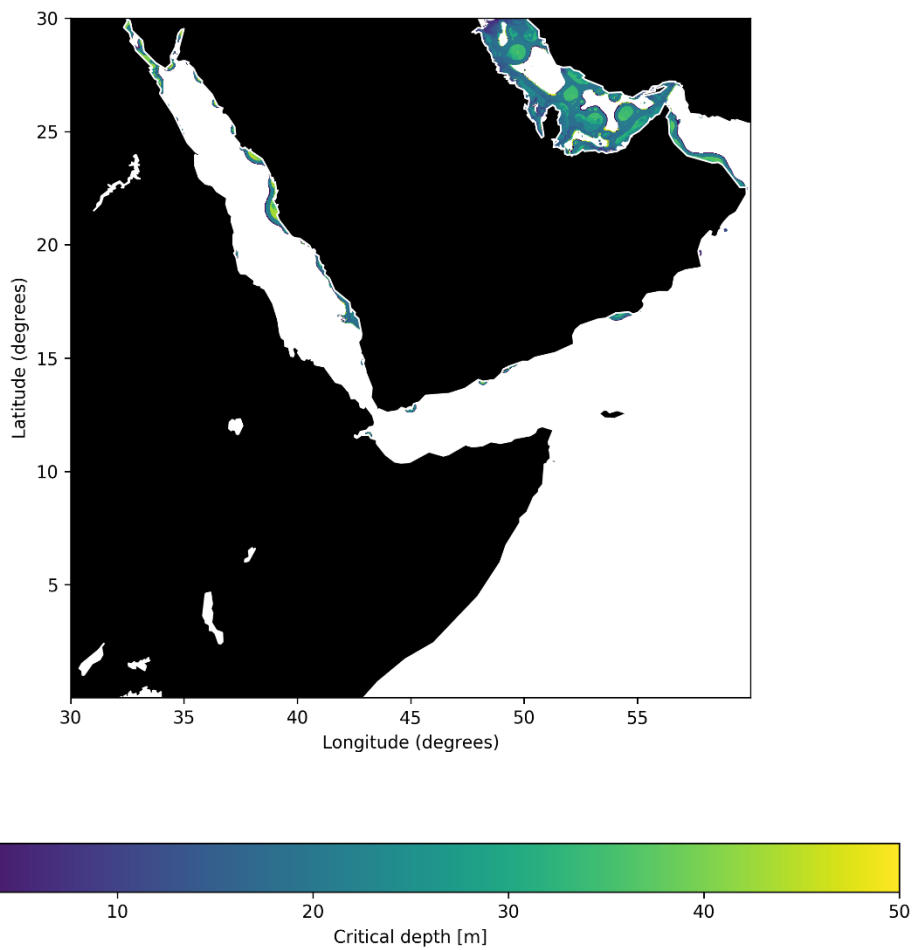


Figure S6. Critical depth (Z_c) for climatological May for northeast Africa and Arabian Peninsula.

Entire dataset can be downloaded in netCDF format from Pangaea

(<https://doi.pangaea.de/10.1594/PANGAEA.929749>)

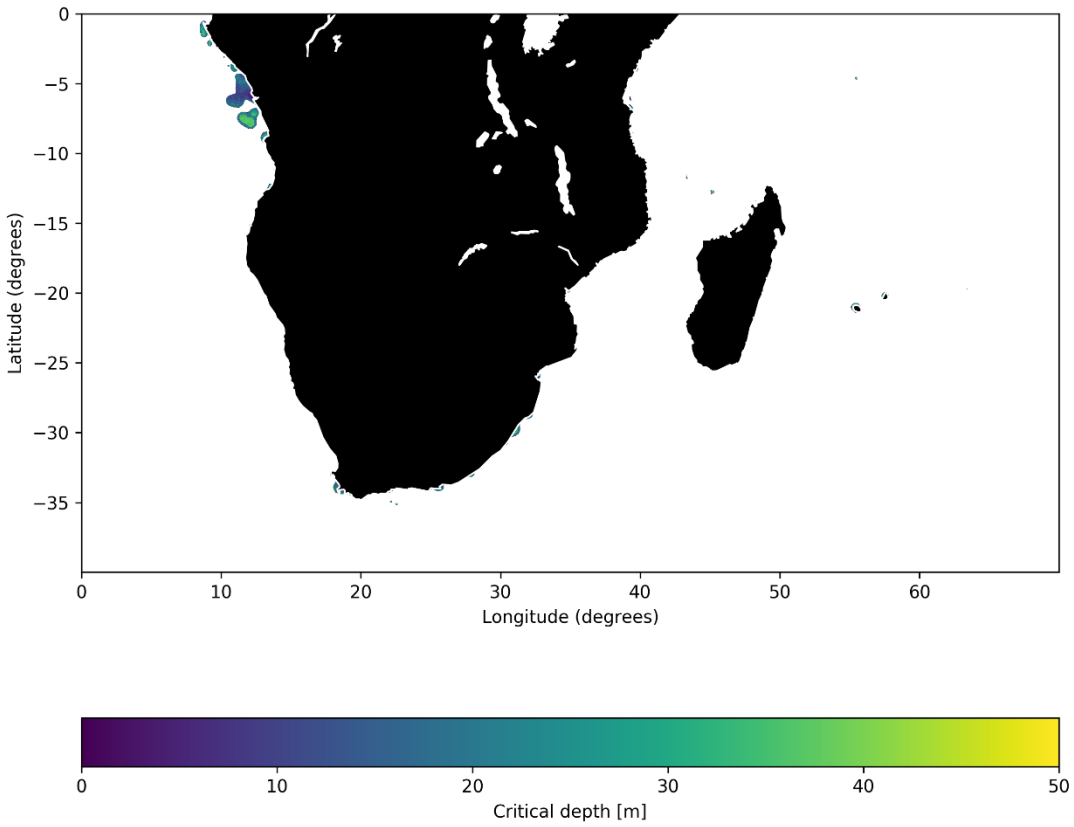


Figure S7. Critical depth (Z_c) for climatological May for southern Africa and Madagascar. Entire dataset can be downloaded in netCDF format from Pangaea (<https://doi.pangaea.de/10.1594/PANGAEA.929749>).

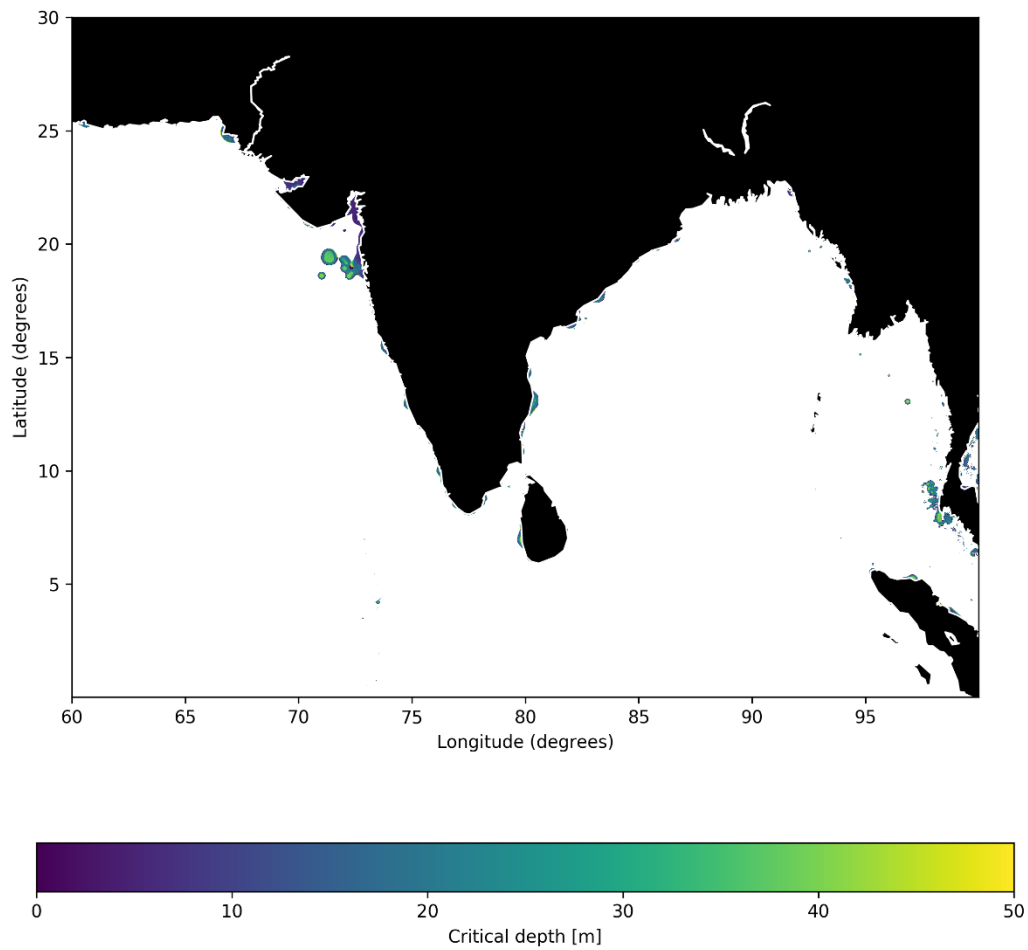


Figure S8. Critical depth (Z_c) for climatological May for northern Indian Ocean. Entire dataset can be downloaded in netCDF format from Pangaea (<https://doi.pangaea.de/10.1594/PANGAEA.929749>).

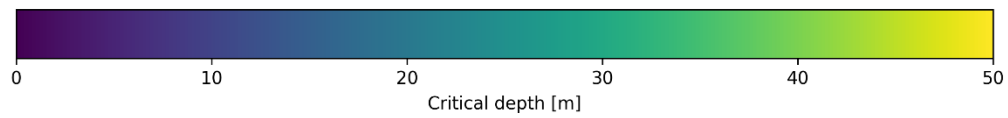
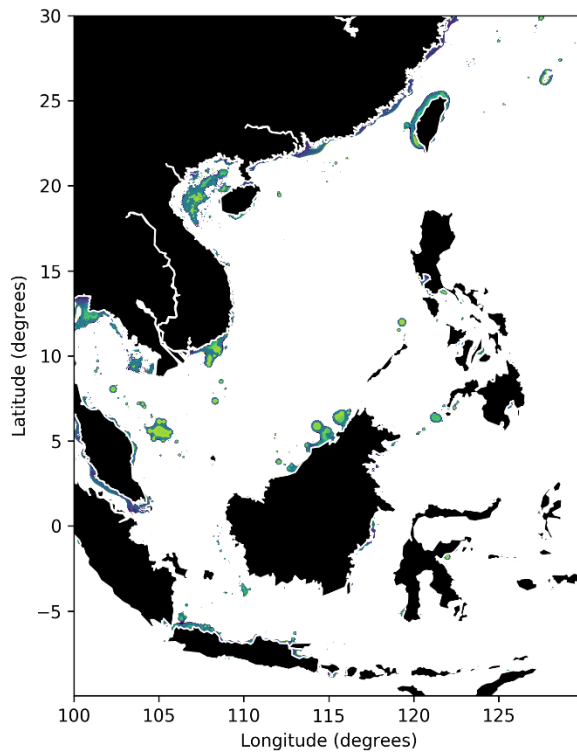


Figure S9. Critical depth (Z_c) for climatological May for Southeast Asia. Entire dataset can be downloaded in netCDF format from Pangaea (<https://doi.pangaea.de/10.1594/PANGAEA.929749>).

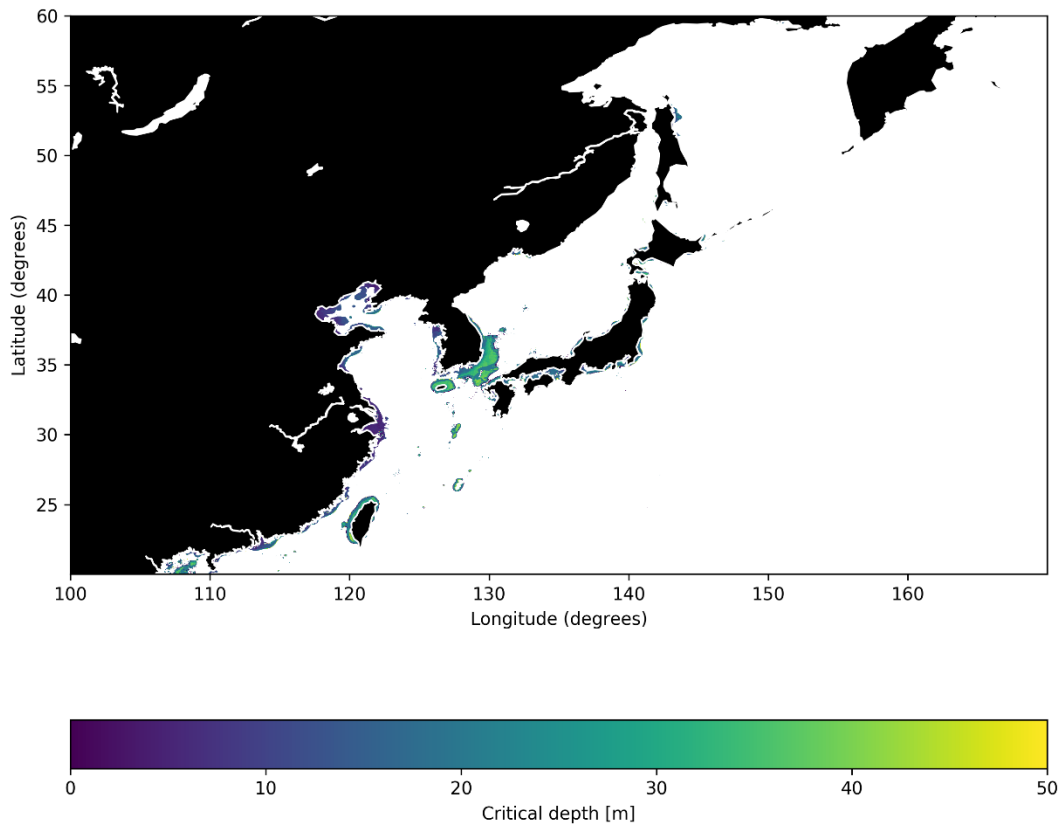


Figure S10. Critical depth (Z_c) for climatological May for northwest Pacific Ocean. Entire dataset can be downloaded in netCDF format from Pangaea (<https://doi.pangaea.de/10.1594/PANGAEA.929749>).

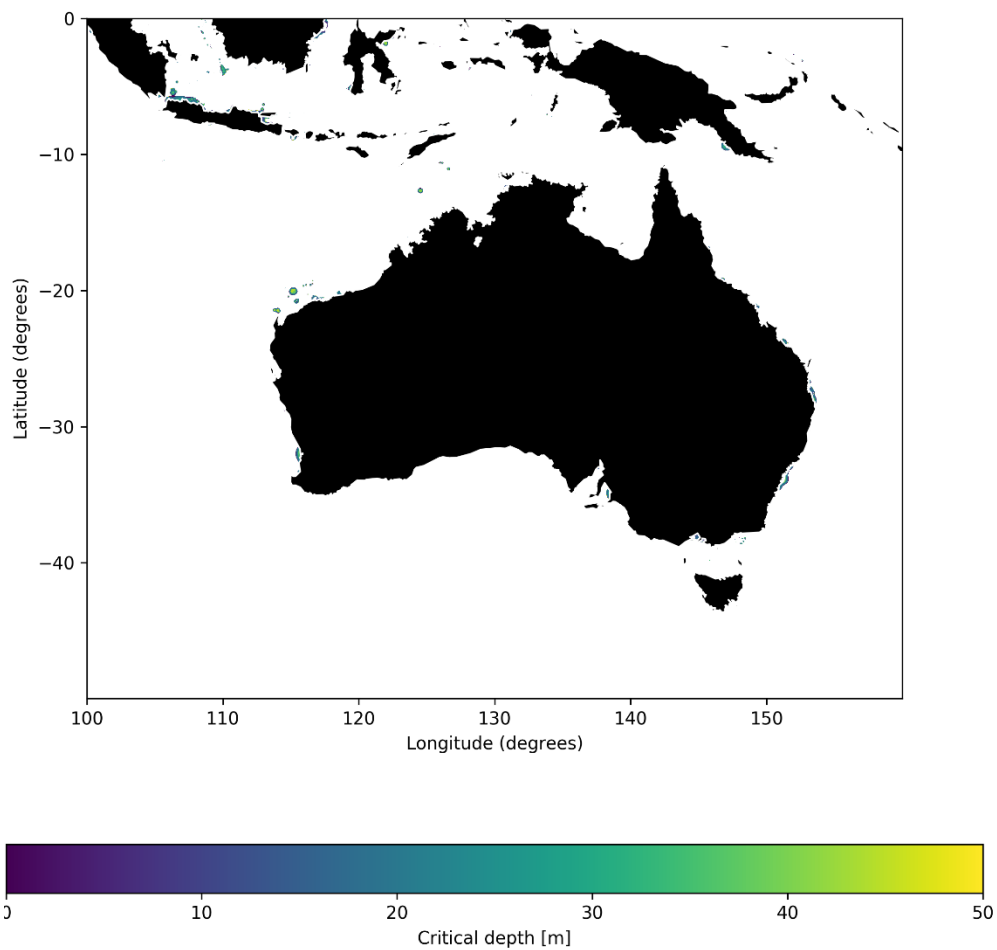


Figure S11. Critical depth (Z_c) for climatological May for Australia and southeast Asia Island chains. Entire dataset can be downloaded in netCDF format from Pangaea (<https://doi.pangaea.de/10.1594/PANGAEA.929749>)